Research Article Vol. 34, No. 7 / July 2017 / Journal of the Optical Society of America A 1201

Journal of the Optical Society of America A
OPTICS, IMAGE SCIENCE, AND VISION

Electromagnetic diffraction theory of refractive axicon lenses

YANGYUNDOU WANG,[1] SHENGGANG YAN,[1] ARI T. FRIBERG,[2] DAVID KUEBEL,[3,4] AND TACO D. VISSER[1,3,5,*]

[1]School of Marine Science and Technology/School of Electronics and Information, Northwestern Polytechnical University, 710072 Xi'an, China
[2]Institute of Photonics, University of Eastern Finland, P.O. Box 111, FI-80101 Joensuu, Finland
[3]Department of Physics and Astronomy, University of Rochester, Rochester, New York 14627, USA
[4]St. John Fisher College, Rochester, New York 14618, USA
[5]Department of Physics and Astronomy, Vrije Universiteit, 1081 HV Amsterdam, The Netherlands
*Corresponding author: tvisser@nat.vu.nl

Received 13 April 2017; revised 24 May 2017; accepted 30 May 2017; posted 30 May 2017 (Doc. ID 292787); published 23 June 2017

We study the field that is produced by a paraxial refractive axicon lens. The results from geometrical optics, scalar wave optics, and electromagnetic diffraction theory are compared. In particular, the axial intensity, the on-axis effective wavelength, the transverse intensity, and the far-zone field are examined. A rigorous electromagnetic diffraction analysis shows that the state of polarization of the incident beam strongly affects the transverse intensity distribution, but not the intensity distribution in the far zone.

OCIS codes: (050.1960) Diffraction theory; (050.1965) Diffractive lenses; (260.2110) Electromagnetic optics; (260.5430) Polarization.

https://doi.org/10.1364/JOSAA.34.001201

1. INTRODUCTION

Axicons [1], sometimes called conical prisms, are optical elements that have rotational symmetry. Whereas ordinary lenses produce a focal spot, axicons generate a focal line, known as the *axicon line image*, which, with increasing distance from the axicon, gradually evolves into a ring-shaped pattern. This makes axicons useful for applications as diverse as imaging with an extended depth of focus [2], surface inspection [3], stimulated Brillouin scattering [4], optical pumping [5], laser drilling [6], optical trapping [7], frequency doubling [8], triangulation [9], optical coherence tomography [10], and corneal surgery [11]. Moreover, they can be used to create so-called nondiffracting Bessel beams [12]. Useful reviews of axicon lenses are presented in Refs. [13–15].

Three types of axicons can be distinguished: diffractive axicons [16–18], reflective axicons [19–22], and refractive axicons [23,24]. In this study, we consider the latter variety. A vector analysis for lenses that produce a converging spherical wavefront has been presented in a well-known study by Richards and Wolf [25]. However, a comprehensive electromagnetic description of refractive axicons, as presented here, has, to the best of our knowledge, not been undertaken yet.

We begin by briefly reviewing several geometrical axicon properties in Section 2. This is followed by a scalar wave analysis in Section 3, in which both the nondiffractive beam properties of the line image and its transition into a ring-shaped intensity profile are examined. In Section 4 we derive expressions for the electromagnetic field that is produced by incident beams whose polarization state is either uniform, e.g., beams that are linearly polarized, or whose polarization state is nonuniform [26], namely, beams with radial or azimuthal polarization. We then apply these formulas in Section 5 to study the on-axis intensity, the effective on-axis wavelength, the transverse field intensity, the state of polarization, and the far-zone field. Because we are dealing with beam-like fields, we will throughout this analysis make use of the paraxial approximation. This justifies neglecting the longitudinal field components.

2. GEOMETRICAL RAYS

A linear, plano-convex refractive axicon, as sketched in Fig. 1, is rotationally symmetric about the z axis and has a cone-shaped form. For holding the cone during manufacturing and use, a cylindrical section is necessary. The axicon is characterized by three parameters: the refractive index n, the base angle α, and the radius a. We consider an axicon that is illuminated by a collection of rays that are all parallel to the z axis. At the conical surface of the axicon, these rays are refracted toward the axis, all under the same angle $\beta - \alpha$. It is seen from Fig. 1 that they are focused along a line that extends over a distance L from the apex of the cone. From Snell's law, we have that $\sin\beta = n \sin\alpha$. Hence the length of the focal line equals

$$L = a \tan\gamma - a \tan\alpha, \tag{1}$$

with the angle γ given by the expression

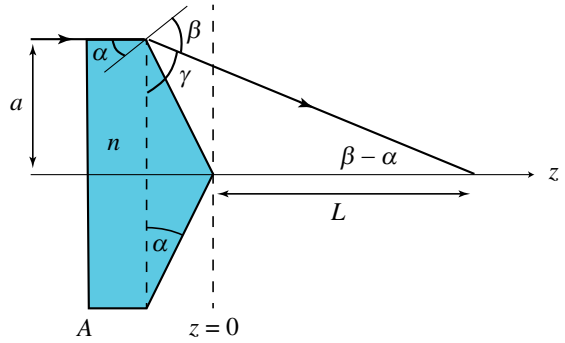

Fig. 1. Refractive axicon with radius a, base angle α, and refractive index n. Rays are normally incident on the front face A. A marginal ray crosses the z axis at a distance L from the apex, which is taken to be in the plane $z = 0$.

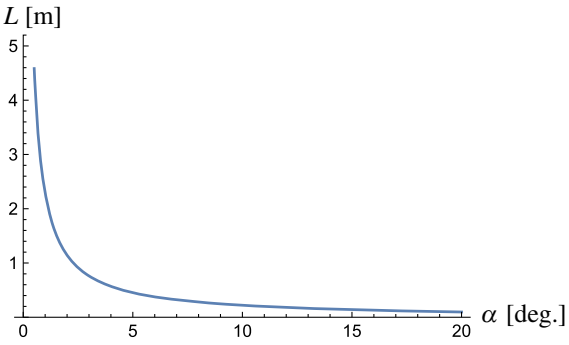

Fig. 2. Length L of the focal line as a function of the base angle α. In this example the refractive index $n = 1.5$, and the axicon radius $a = 2$ cm.

$$\gamma = 90° - \beta + \alpha. \tag{2}$$

The length of the focal line versus the base angle α is shown in Fig. 2. It is seen that for applications in which a long focal line is necessary, the base angle must be quite small. We will from here on restrict ourselves to this paraxial regime.

We assume that the incident field has a Gaussian intensity profile, i.e.,

$$I^{(\mathrm{in})}(\boldsymbol{\rho}) = I_0 \exp(-2\rho^2/w_0^2), \tag{3}$$

with I_0 and w_0 positive constants, and $\rho = |\boldsymbol{\rho}| = |(x, y)|$ being the radial distance from the z axis. In order to calculate the axial intensity distribution, we consider a thin ring on the front face A, with inner radius ρ and outer radius $\rho + \delta\rho$. The power flow through the ring is

$$P(\rho) = I_0 \exp(-2\rho^2/w_0^2) 2\pi\rho\delta\rho. \tag{4}$$

The transmitted portion of this power is projected onto the z axis between the two positions

$$L_1 = \rho(\tan\gamma - \tan\alpha), \tag{5}$$

$$L_2 = (\rho + \delta\rho)(\tan\gamma - \tan\alpha), \tag{6}$$

where we have used Eq. (1) with the variable a replaced by the radial distances ρ and $\rho + \delta\rho$, respectively. The rays carrying this power make an angle $\beta - \alpha$ with the z axis. If we define the length $\delta L = L_2 - L_1$, then the axial intensity or "power per unit length" equals

$$\frac{P(\rho)}{\delta L} T_1^2(\omega) T_2^2(\omega) \cos(\beta - \alpha) = \frac{2\pi I_0 T_1^2(\omega) T_2^2(\omega) \cos(\beta - \alpha)}{\tan\gamma - \tan\alpha} \rho \exp(-2\rho^2/w_0^2). \tag{7}$$

Here $T_1(\omega)$ and $T_2(\omega)$ are the amplitude transmission coefficients at frequency ω of the air-glass interface for normal incidence, and of the glass-air interface for incidence at an angle α, respectively. From Eq. (1) we find that $z = \rho(\tan\gamma - \tan\alpha)$, and thus the axial intensity is given by the formula

$$I(z) = D_1 z \exp[-2z^2/w_0^2(\tan\gamma - \tan\alpha)^2], \tag{8}$$

where we introduced the symbol D_1, with

$$D_1 = \frac{2\pi I_0 T_1^2(\omega) T_2^2(\omega) \cos(\beta - \alpha)}{(\tan\gamma - \tan\alpha)^2}. \tag{9}$$

This factor is independent of the position z. Note that this geometrical model predicts a nonzero field on-axis only when $0 \le z \le L$. In the next section, we will compare the prediction of Eq. (8) with the result of a scalar analysis.

3. SCALAR FIELDS

Let us next consider a plane, monochromatic scalar wave of frequency ω with a Gaussian amplitude distribution that is propagating in the positive z direction. The wave is normally incident on the front face A of the axicon.

In the space-frequency domain, this wave can be represented as

$$U^{(\mathrm{in})}(\boldsymbol{\rho}, \omega) = U_0(\omega) \exp(-\rho^2/w_0^2), \tag{10}$$

where $U_0(\omega)$ denotes the spectral amplitude, with $|U_0(\omega)|^2 = I_0$, and w_0 the beam width in the plane A (see Fig. 3). The base angle α is taken to be quite small, which justifies using the paraxial approximation. In order to calculate the field in the output plane $z = 0$, we notice that at position $Q'(\boldsymbol{\rho}, 0)$ the field has traveled a length d through air, namely,

$$d \approx \rho \tan\alpha \approx \rho\alpha. \tag{11}$$

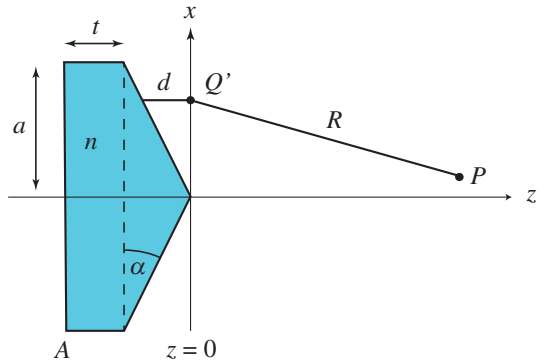

Fig. 3. Paraxial refractive axicon with radius a, base angle α, and refractive index n. A plane wave with a Gaussian amplitude distribution is normally incident on the front face A. The thickness of the cylindrical base is denoted by t, and $z = 0$ indicates the output plane.

The phase difference Δ between the field at Q' and that on the z axis is therefore

$$\Delta = (1 - n)kd = (1 - n)k\rho\alpha, \tag{12}$$

where k denotes the free-space wavenumber associated with frequency ω. We thus find that the output field in the plane $z = 0$ is related to the incident field in the entrance plane A by the formula

$$U^{(\mathrm{out})}(\boldsymbol{\rho}, \omega) = T(\rho, \omega)U^{(\mathrm{in})}(\boldsymbol{\rho}, \omega), \tag{13}$$

with $T(\rho, \omega)$ given by the expression

$$T(\rho, \omega) = C(\omega)\exp[\mathrm{i}k(1 - n)\rho\alpha] \tag{14}$$

and with the factor $C(\omega)$ being independent of ρ, namely,

$$C(\omega) = T_1(\omega)T_2(\omega)\exp(\mathrm{i}knt). \tag{15}$$

Here $T_1(\omega)$ and $T_2(\omega)$ are the transmission coefficients described in relation with Eq. (7), and t is the thickness of the cylindrical axicon base.

The field at a position $P(\mathbf{r})$ behind the lens is, according to the Huygens–Fresnel principle ([27], Chap. 8), given by the expression

$$U(\mathbf{r}, \omega) = -\frac{\mathrm{i}}{\lambda}\iint_{z=0} U^{(\mathrm{out})}(\boldsymbol{\rho}', \omega)\frac{e^{\mathrm{i}kR}}{R}\mathrm{d}^2\rho', \tag{16}$$

where $R = [z^2 + (x - \xi)^2 + (y - \eta)^2]^{1/2}$ is the distance between $P(x, y, z)$ and $Q'(\xi, \eta, 0)$, and λ is the free-space wavelength. Using the Fresnel approximation, together with Eq. (13), this diffraction integral can be expressed as

$$\begin{aligned} U(x, y, z) = &-\frac{\mathrm{i}CU_0}{\lambda z}\exp(\mathrm{i}kz) \\ &\times \iint_{z=0} \exp\left[\mathrm{i}k(1 - n)\sqrt{\xi^2 + \eta^2}\alpha\right] \\ &\times \exp[-(\xi^2 + \eta^2)/w_0^2] \\ &\times \exp\left\{\mathrm{i}\frac{k}{2z}[(x - \xi)^2 + (y - \eta)^2]\right\}\mathrm{d}\xi\mathrm{d}\eta, \end{aligned} \tag{17}$$

where, for brevity, the ω dependence has been omitted. In cylindrical coordinates

$$\boldsymbol{\rho}' = (\xi, \eta) = \rho'(\cos\mu, \sin\mu), \tag{18}$$

$$\boldsymbol{\rho} = (x, y) = \rho(\cos\delta, \sin\delta), \tag{19}$$

the field at P can be written as

$$\begin{aligned} U(\boldsymbol{\rho}, z) = &-\frac{\mathrm{i}CU_0}{\lambda z}\exp(\mathrm{i}kz)\exp\left(\mathrm{i}\frac{k}{2z}\rho^2\right) \\ &\times \int_0^{2\pi}\int_0^a \exp[\mathrm{i}k(1 - n)\rho'\alpha]\exp(-\rho'^2/w_0^2) \\ &\times \exp\left(\mathrm{i}\frac{k}{2z}\rho'^2\right) \\ &\times \exp\left[-\mathrm{i}\frac{k\rho\rho'}{z}\cos(\mu - \delta)\right]\rho'\mathrm{d}\rho'\mathrm{d}\mu. \end{aligned} \tag{20}$$

The integral over the angle μ is independent of δ, and hence we obtain the formula

$$\begin{aligned} U(\boldsymbol{\rho}, z) = &-\frac{\mathrm{i}2\pi CU_0}{\lambda z}\exp(\mathrm{i}kz)\exp\left(\mathrm{i}\frac{k}{2z}\rho^2\right) \\ &\times \int_0^a \exp[\mathrm{i}k(1 - n)\rho'\alpha]\exp\left(\mathrm{i}\frac{k}{2z}\rho'^2\right) \\ &\times \exp(-\rho'^2/w_0^2)J_0\left(\frac{k\rho\rho'}{z}\right)\rho'\mathrm{d}\rho', \end{aligned} \tag{21}$$

with J_0 a Bessel function of the first kind of order zero. We note that the field is rotationally symmetric about the z axis, i.e., it depends on $\rho = |\boldsymbol{\rho}|$. The intensity follows from the definition

$$I(\rho, z) = |U(\rho, z)|^2, \tag{22}$$

as is customary in scalar optics.

The oscillatory integral in Eq. (21) can be evaluated numerically, but it is instructive to find an approximate solution by using the method of stationary phase ([28], Section 3.3). If we consider only the contribution of the interior stationary point, which means that the edge contribution is ignored, the result for $0 < z < L$ is (see Appendix A for details)

$$\begin{aligned} U(\rho, z) = &-\mathrm{i}CU_0(2\pi kz)^{1/2}(n - 1)\alpha\exp(\mathrm{i}\pi/4)\exp(\mathrm{i}kz) \\ &\times \exp(\mathrm{i}k\rho^2/2z)\exp[-\mathrm{i}kz(n - 1)^2\alpha^2/2] \\ &\times \exp[-z^2(1 - n)^2\alpha^2/w_0^2]J_0[(n - 1)k\rho\alpha]. \end{aligned} \tag{23}$$

For the intensity we hence find that

$$\begin{aligned} I(\rho, z) = &D_2 z\exp[-2z^2(1 - n)^2\alpha^2/w_0^2] \\ &\times \{J_0[(n - 1)k\rho\alpha]\}^2, \end{aligned} \tag{24}$$

where the constant D_2 is independent of position and given by the expression

$$D_2 = C^2 I_0 2\pi k(n - 1)^2\alpha^2. \tag{25}$$

Before discussing the implications of these diffraction integrals, it is important to note that whereas Eq. (21) is valid for all axial positions z, Eq. (23) only applies for the interval $0 \le z \le L$. When z is beyond the focal line, the method of stationary phase, just like the geometrical model, predicts an axial field that is identically zero.

A. Axial Intensity

The axial intensity distribution produced by an axicon is shown in Fig. 4 based on the three different models we have discussed so far: geometrical optics [Eq. (8)], scalar wave optics using the full diffraction integral [Eq. (21)], and scalar wave optics using the method of stationary phase [Eq. (24)]. For the choice of parameters used in panel (a), the three curves are virtually indistinguishable. The intensity is seen to first rise, after which an exponential decay sets in. The length of the focal line as calculated from Eq. (1), $L = 1.15$ m in this case. The beam waist w_0 was taken to be less than the axicon radius a. Neglecting the boundary contribution, as is done in the stationary phase expression Eq. (24), is then justified. However, when the beam waist and the axicon radius are equal, as illustrated in panel (b), the edge contribution becomes significant. The diffraction integral of Eq. (21), in which the edge contribution is *not* neglected, now predicts an intensity with a modulation with increasing size and decreasing periodicity, followed by a steep decline to zero. That the boundary contribution leads to an

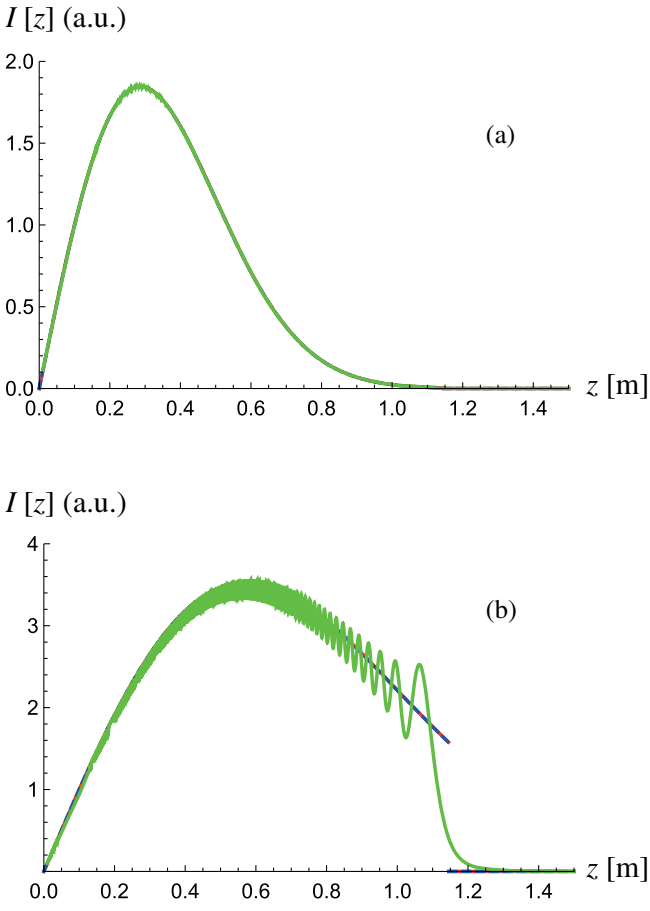

Fig. 4. Normalized intensity distribution along the z axis as given by geometrical optics [Eq. (8)] (blue), wave optics using the full diffraction integral [Eq. (21)] (green), and wave optics employing the method of stationary phase [Eq. (24)] (red). In panel (a) the beam waist $w_0 = 0.5$ cm, which is smaller than the axicon radius. In panel (b) $w_0 = 1$ cm, which is equal to the axicon radius. In both these examples, the refractive index $n = 1.5$, the base angle $\alpha = 1°$, the axicon radius $a = 1$ cm, and the wavelength $\lambda = 632.8$ nm.

oscillatory intensity has been discussed previously, e.g., in Refs. [17] and [29]. This behavior is in stark contrast with Eqs. (8) and (24). These two formulas both still predict a smooth intensity distribution, but now with a discontinuous drop to zero at the end of the focal line ($z = L$).

B. Transverse Intensity

The normalized transverse intensity distribution, as given by Eq. (24), is seen to be

$$I(\rho) = \{J_0[(n-1)k\rho\alpha]\}^2, \qquad (z < L), \tag{26}$$

which is independent of z. It is this ability of axicons to produce "diffraction-free" or "propagation-invariant" Bessel beams that has attracted much attention [30–34]. Because Eq. (26) is only valid when $z < L$, it cannot be used to investigate the transition of the axicon line image to a ring-shaped profile. To that end, we therefore use Eq. (21) which, in contrast to Eq. (26), does *not* rely on the stationary phase approximation. In Fig. 5, the transverse intensity is shown in different cross sections. The

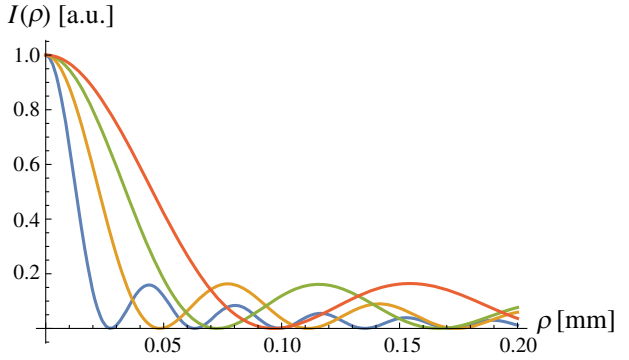

Fig. 5. Normalized transverse intensity distribution according to Eq. (21) in different planes. From left to right, $z = 1$ m, 2 m, 3 m, and 4 m. In these examples $\lambda = 632.8$ nm, $\alpha = 1°$, $w_0 = 1$ cm, $a = 1$ cm, and $n = 1.5$.

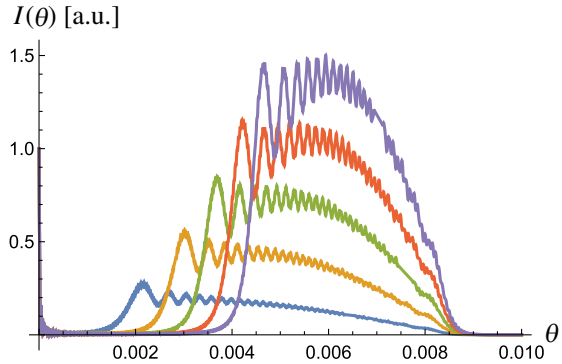

Fig. 6. Transverse intensity distribution according to Eq. (21), normalized to unity at $\theta = 0$, as a function of the polar angle, in different cross sections. From left to right, $z = 1.4$ m, 1.6 m, 1.8 m, 2.0 m, and 2.2 m. All other parameters are the same as in Fig. 5.

left-most curve ($z = 1$ m), is practically identical with the J_0^2 prediction of Eq. (26). For values larger than the focal line length $L = 1.14$ m [see Eq. (1)], the distribution gets progressively broader. We note that, for clarity, all curves in Fig. 5 are normalized to 1 at $\rho = 0$. In reality, obviously, the axial intensity will decrease when z gets larger.

The gradual broadening of the central transverse peak is accompanied by the onset of sidelobes, which eventually leads to a ring-like intensity profile. This is shown in Fig. 6, where, because the peaks begin to cluster around the same angle, the horizontal axis now represents the polar angle θ, rather than the radial distance ρ. The sidelobes, positioned between $\theta = 0.002$ and $\theta = 0.008$, have a maximum intensity that increases with increasing z. Gradually, this maximum begins to exceed the unit intensity on the axis ($\theta = 0$).

The influence of the beam waist size w_0 can be examined by increasing its value from 1 cm to 1 m. The result is shown in Fig. 7, in which it can be seen that the position of the maxima remains the same, but the secondary sidelobes are now more suppressed.

For even larger distances, as plotted in Fig. 8, these sidelobes get narrower, and a ring-like field develops around the angle

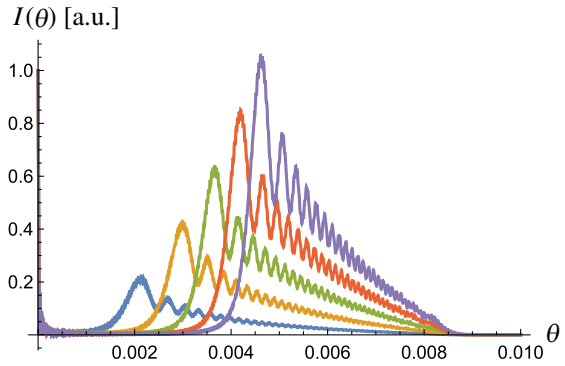

Fig. 7. Transverse intensity distribution according to Eq. (21), normalized to unity at $\theta = 0$, as a function of the polar angle, in different cross sections. From left to right, $z = 1.4$ m, 1.6 m, 1.8 m, 2.0 m, and 2.2 m. The beam waist w_0 is now increased to 1 m, from 1 cm in Figs. 5 and 6. All the other parameters are the same as in Fig. 5.

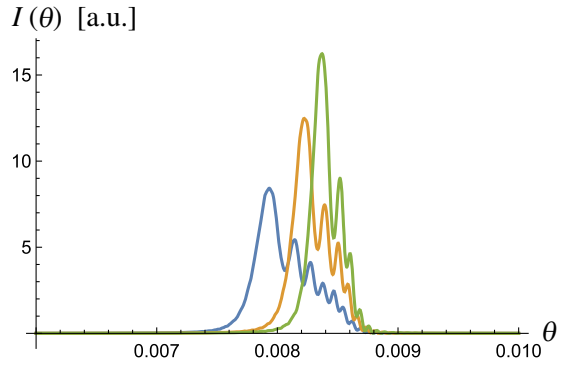

Fig. 8. Transverse intensity distribution according to Eq. (21), normalized to unity at $\theta = 0$, as a function of the polar angle, in different cross sections. From left to right, $z = 10$ m, 15 m, and 20 m. The beam waist $w_0 = 1$ m. All other parameters are the same as in Fig. 5.

$\theta = \beta - \alpha = 0.0087$, which is precisely the geometrical angle of refraction shown in Fig. 1. Of course, the far-zone field (the field at infinity) can be brought to the focal plane of a paraxial lens. Notice that in Figs. 5–8 the same normalization is used. This means, for example, that for the right-most curve in Fig. 8 ($z = 20$ m), the intensity of the ring-like sidelobe is about 16 times higher than that of the field on-axis.

4. ELECTROMAGNETIC FIELDS

In this section, we analyze two types of incident electromagnetic beams, namely, beams with a uniform polarization, i.e., beams whose state of polarization is the same at all points in a cross section, and radially and azimuthally polarized beams, which are nonuniformly polarized.

A. Linear Polarization

We begin by assuming a monochromatic, normally incident field that is linearly polarized along the x direction, i.e., a field of the form

$$\mathbf{E}^{(\mathrm{in})}(\mathbf{r}) = E_0 \hat{\mathbf{x}} e^{ik(z-\epsilon)} = E_0 (1,0,0)^T e^{ik(z-\epsilon)}, \tag{27}$$

with $E_0 > 0$, $k\epsilon$ a phase constant, and T denoting the transpose. We note that this incident field has a constant amplitude, in contrast to the Gaussian fields that were discussed in earlier sections. The Fresnel transmission coefficient T_1 for normal incidence at the front face A gives rise to an overall amplitude factor that is independent of position, i.e., ([35], Section 7.3)

$$T_1 = \frac{2}{n+1}. \tag{28}$$

As can be seen from Fig. 3, the field travels a distance $t + \alpha(a - \rho)$ from the entrance plane A to the inside of the conical surface. Hence the field there, indicated by the superscript (–), equals

$$\mathbf{E}^{(-)}(\mathbf{r}) = E_0 T_1 e^{ik(z-\epsilon)} e^{ikn[t+\alpha(a-\rho)]} (1,0,0)^T. \tag{29}$$

The inward normal vector of the cone is given by the expression

$$\hat{\mathbf{n}} = -(\sin\alpha\cos\phi, \sin\alpha\sin\phi, \cos\alpha)^T, \tag{30}$$

where the caret symbol denotes a unit vector. We define the vector $\mathbf{s}$, which is normal to the plane of incidence at the conical surface, as

$$\mathbf{s} = \hat{\mathbf{z}} \times \hat{\mathbf{n}}, \tag{31}$$

$$= (\sin\alpha\sin\phi, -\sin\alpha\cos\phi, 0)^T. \tag{32}$$

The vector $\hat{\mathbf{p}}$, which lies in the plane of incidence and is also perpendicular to the wave vector within the axicon, is defined as

$$\hat{\mathbf{p}} = \hat{\mathbf{z}} \times \hat{\mathbf{s}}, \tag{33}$$

$$= (\cos\phi, \sin\phi, 0)^T. \tag{34}$$

The electric field vector can now be decomposed into an s- and a p-polarized part by writing

$$\mathbf{E}^{(-)}(\rho,\phi) = \mathbf{E}_s^{(-)}(\rho,\phi) + \mathbf{E}_p^{(-)}(\rho,\phi), \tag{35}$$

with

$$\mathbf{E}_s^{(-)}(\rho,\phi) = [\mathbf{E}^{(-)}(\rho,\phi)\cdot\hat{\mathbf{s}}]\hat{\mathbf{s}}, \tag{36}$$

$$= \Lambda(\rho)(\sin^2\phi, -\cos\phi\sin\phi, 0)^T, \tag{37}$$

$$\mathbf{E}_p^{(-)}(\rho,\phi) = [\mathbf{E}^{(-)}(\rho,\phi)\cdot\hat{\mathbf{p}}]\hat{\mathbf{p}}, \tag{38}$$

$$= \Lambda(\rho)(\cos^2\phi, \cos\phi\sin\phi, 0)^T, \tag{39}$$

and where we introduced the abbreviation

$$\Lambda(\rho) = E_0 T_1 e^{ik(z-\epsilon)} e^{ikn[t+\alpha(a-\rho)]}. \tag{40}$$

These two field components are transmitted with their respective Fresnel coefficients, T_s and T_p, for which we have ([27], Section 1.5.2)

$$T_s = \frac{2n\cos\alpha}{n\cos\alpha + \sqrt{1 - n^2\sin^2\alpha}}, \tag{41}$$

$$T_p = \frac{2n\cos\alpha}{\cos\alpha + n\sqrt{1 - n^2\sin^2\alpha}}. \tag{42}$$

Whereas the s-polarized part remains otherwise unchanged, the p-polarized part of the electric field is, according to Snell's law, also rotated over an angle $\beta - \alpha$ around the vector $\mathbf{s}$ (see Fig. 1), with

$$\sin\beta = n\sin\alpha. \tag{43}$$

If we now introduce a vector $\hat{\mathbf{q}}$ by defining

$$\hat{\mathbf{q}} = (\cos(\beta-\alpha)\cos\phi, \cos(\beta-\alpha)\sin\phi, \sin(\beta-\alpha))^T, \tag{44}$$

it is readily verified that

$$\hat{\mathbf{q}}\cdot\hat{\mathbf{s}} = 0 \tag{45}$$

and that

$$\hat{\mathbf{q}}\cdot\hat{\mathbf{p}} = \cos(\beta-\alpha). \tag{46}$$

This demonstrates that the rotation indeed transforms the vector $\hat{\mathbf{p}}$ into $\hat{\mathbf{q}}$. Hence the field at the right-hand side of the conical surface, indicated by the superscript $(+)$, equals

$$\mathbf{E}^{(+)}(\rho,\phi) = T_s[\mathbf{E}^{(-)}(\rho,\phi)\cdot\hat{\mathbf{s}}]\hat{\mathbf{s}} + T_p[\mathbf{E}^{(-)}(\rho,\phi)\cdot\hat{\mathbf{p}}]\hat{\mathbf{q}}, \tag{47}$$

$$= T_s\Lambda(\rho)\begin{pmatrix}\sin^2\phi\\ -\cos\phi\sin\phi\\ 0\end{pmatrix} + T_p\Lambda(\rho)\begin{pmatrix}\cos(\beta-\alpha)\cos^2\phi\\ \cos(\beta-\alpha)\cos\phi\sin\phi\\ \sin(\beta-\alpha)\cos\phi\end{pmatrix}. \tag{48}$$

The assumption of paraxiality allows us to neglect the relatively small z component of the electric field in Eq. (48) that is introduced by refraction of the p-polarized part. In addition, we note that the two Fresnel coefficients are related by the expression ([27], Section 1.5.2)

$$T_p\cos(\beta-\alpha) = T_s. \tag{49}$$

On making use of this in Eq. (48), it follows that the expression for the x component simplifies, and that the y component vanishes, and hence we find that

$$\mathbf{E}^{(+)}(\rho,\phi) = T_s\Lambda(\rho)(1,0,0)^T. \tag{50}$$

The field on the right-hand side of the axicon surface propagates to the output plane $z=0$. As indicated by Eq. (11), this involves a distance $d=\rho\alpha$ in air, giving rise to a phase factor of $\exp(ik\rho\alpha)$. Hence the field $\mathbf{E}^{(\mathrm{out})}(\rho,\phi)$ in the output plane is given by the expression

$$\mathbf{E}^{(\mathrm{out})}(\rho,\phi) = \exp(ik\rho\alpha)\mathbf{E}^{(+)}(\rho,\phi), \tag{51}$$

$$= \exp(ik\rho\alpha)T_s\Lambda(\rho)(1,0,0)^T. \tag{52}$$

We note that this output field has no ϕ dependence.

Having established the field in the output plane, the field in the half-space $z>0$ can be calculated by using the diffraction formula

$$\mathbf{E}(\mathbf{r}) = \frac{1}{2\pi}\nabla\times\int_{z'=0}[\hat{\mathbf{z}}\times\mathbf{E}^{(\mathrm{out})}(\mathbf{r}')]\frac{e^{ikR}}{R}\mathrm{d}^2r', \tag{53}$$

where $R=|\mathbf{r}-\mathbf{r}'|$. We note that Eq. (53) is derived in ([35], Section 10.7) for apertures in a plane conducting screen. However, it is valid for any planar surface, as is shown in ([36], pp. 218–221). On substituting Eq. (52) into Eq. (53), we find that

$$\mathbf{E}(\mathbf{r}) = \frac{1}{2\pi}\int_{z'=0}\begin{pmatrix}-E_x^{(\mathrm{out})}(\mathbf{r}')\partial_z\\ 0\\ E_x^{(\mathrm{out})}(\mathbf{r}')\partial_x\end{pmatrix}\frac{e^{ikR}}{R}\mathrm{d}^2r'. \tag{54}$$

Whereas in Eq. (48) the z component was introduced by refraction, in Eq. (54) it arises as a result from diffraction. Differentiation with respect to z of the factor $\exp(ikR)/R$ introduces a prefactor z, whereas differentiation with respect to x leads to a factor $x-x'$. Therefore the z component of the diffracted field drops off quickly with increasing z, and may therefore be neglected. Hence we find that

$$\mathbf{E}(\mathbf{r}) = \frac{-T_s}{2\pi}\hat{\mathbf{x}}\int_{z'=0}e^{ik\rho'\alpha}\Lambda(\rho')\partial_z\frac{e^{ikR}}{R}\mathrm{d}^2r'. \tag{55}$$

We will make use of this expression in Section 5.

B. Uniform Polarization

We have thus far considered an incident beam that is linearly polarized along the x direction. Let us now generalize Eq. (27) to beams with an arbitrary, but uniform state of polarization, namely,

$$\mathbf{E}^{(\mathrm{in})}(\mathbf{r}) = E_0\hat{\mathbf{u}}e^{ik(z-\epsilon)}, \tag{56}$$

where

$$\hat{\mathbf{u}} = A_x\hat{\mathbf{x}} + A_y\hat{\mathbf{y}}, \tag{57}$$

and with A_x and A_y complex-valued constants such that $|A_x|^2+|A_y|^2=1$. For example, $A_y = iA_x$ represents a circularly polarized beam. Because the axicon is a linear system with rotational symmetry, the resulting field in the half-space $z>0$ can be found by simply adding the contributions of both field components of Eq. (57), i.e.,

$$\mathbf{E}(\mathbf{r}) = -\frac{1}{2\pi}A_xT_s\hat{\mathbf{x}}\int_{z'=0}e^{ik\rho'\alpha}\Lambda(\rho')\partial_z\frac{e^{ikR}}{R}\mathrm{d}^2r' - \frac{1}{2\pi}A_yT_s\hat{\mathbf{y}}\int_{z'=0}e^{ik\rho'\alpha}\Lambda(\rho')\partial_z\frac{e^{ikR}}{R}\mathrm{d}^2r'. \tag{58}$$

This expression demonstrates that the x and y field components everywhere in the half-space $z>0$ have the same amplitude and phase relation (given by A_x and A_y) as the two components of the incident field. We therefore conclude that the state of polarization of the diffracted field is the same as that of the uniformly polarized incident beam that generates it.

We next turn our attention to two types of beams with a nonuniform state of polarization.

C. Radial Polarization

Consider a monochromatic, normally incident beam that is radially polarized, i.e.,

$$\mathbf{E}^{(\mathrm{in})}(\mathbf{r}) = E_0\hat{\boldsymbol{\rho}}e^{ik(z-\epsilon)}, \tag{59}$$

$$= E_0(\cos\phi, \sin\phi, 0)^T e^{ik(z-\epsilon)}. \tag{60}$$

The field at the left-hand side of the axicon surface is now

$$\mathbf{E}^{(-)}(\mathbf{r}) = E_0T_1e^{ik(z-\epsilon)}e^{ikn[t+\alpha(a-\rho)]}\hat{\boldsymbol{\rho}}, \tag{61}$$

$$= \Lambda(\rho)(\cos\phi, \sin\phi, 0)^T, \tag{62}$$

with $\Lambda(\rho)$ defined by Eq. (40). The s-polarized part is zero, i.e.,

$$\mathbf{E}^{(-)}(\rho,\phi)\cdot\hat{\mathbf{s}} = 0, \tag{63}$$

whereas the p-polarized part equals

$$\mathbf{E}^{(-)}(\rho,\phi)\cdot\hat{\mathbf{p}}=\Lambda(\rho). \tag{64}$$

The field at the right-hand side of the axicon surface is therefore

$$\mathbf{E}^{(+)}(\rho,\phi)=T_p[\mathbf{E}^{(-)}(\rho,\phi)\cdot\hat{\mathbf{p}}]\hat{\mathbf{q}}, \tag{65}$$

$$=T_p\Lambda(\rho)\begin{pmatrix}\cos(\beta-\alpha)\cos\phi\\ \cos(\beta-\alpha)\sin\phi\\ \sin(\beta-\alpha)\end{pmatrix}. \tag{66}$$

If we again neglect the weak z component and make use of Eq. (49), we find that the output field in the plane $z=0$ is given by the formula

$$\mathbf{E}^{(\mathrm{out})}(\rho,\phi)=\exp(ik\rho\alpha)\mathbf{E}^{(+)}(\rho,\phi), \tag{67}$$

$$=T_s\Lambda(\rho)\exp(ik\rho\alpha)(\cos\phi,\sin\phi,0)^T. \tag{68}$$

We will momentarily analyze the diffracted field produced by a radially polarized beam by substituting Eq. (68) into Eq. (53).

D. Azimuthal Polarization

Consider a monochromatic, normally incident beam that is azimuthally polarized, i.e.,

$$\mathbf{E}^{(\mathrm{in})}(\mathbf{r})=E_0\hat{\boldsymbol{\phi}}e^{ik(z-\epsilon)}, \tag{69}$$

$$=E_0(-\sin\phi,\cos\phi,0)^T e^{ik(z-\epsilon)}. \tag{70}$$

The field at the left-hand side of the axicon surface is then

$$\mathbf{E}^{(-)}(\mathbf{r})=E_0T_1e^{ik(z-\epsilon)}e^{ikn[t+\alpha(a-\rho)]}\hat{\boldsymbol{\phi}}$$

$$=\Lambda(\rho)(-\sin\phi,\cos\phi,0)^T. \tag{71}$$

The s-polarized part is

$$\mathbf{E}^{(-)}(\rho,\phi)\cdot\hat{\mathbf{s}}=-\Lambda(\rho), \tag{72}$$

whereas the p-polarized part now equals zero, i.e.,

$$\mathbf{E}^{(-)}(\rho,\phi)\cdot\hat{\mathbf{p}}=0. \tag{73}$$

The field at the right-hand side of the axicon surface is therefore

$$\mathbf{E}^{(+)}(\rho,\phi)=T_s[\mathbf{E}^{(-)}(\rho,\phi)\cdot\hat{\mathbf{s}}]\hat{\mathbf{s}}, \tag{74}$$

$$=-T_s\Lambda(\rho)(\sin\phi,-\cos\phi,0)^T, \tag{75}$$

and hence the output field in the plane $z=0$ is given by the formula

$$\mathbf{E}^{(\mathrm{out})}(\rho,\phi)=\exp(ik\rho\alpha)\mathbf{E}^{(+)}(\rho,\phi), \tag{76}$$

$$=-T_s\Lambda(\rho)\exp(ik\rho\alpha)(\sin\phi,-\cos\phi,0)^T. \tag{77}$$

We will analyze the field produced by an azimuthally polarized beam by substituting Eq. (77) into Eq. (53).

5. ELECTROMAGNETIC FIELDS GENERATED BY AXICONS

We are now in a position to compare the on-axis field, the transverse intensity distribution, and the intensity in the far zone for each of the three types of polarization that were discussed in the previous section.

A. Axial Intensity

For linear polarization we find, by applying Eq. (55) to points on the z axis and using polar coordinates, for the only nonzero component of the electric field the expression

$$E_x(0,0,z)=\frac{z}{2\pi}T_s\int_0^a\int_0^{2\pi}\exp[ik\rho'\alpha]\Lambda(\rho')\times\frac{e^{ikR}}{R^2}\left[\frac{1}{R}-ik\right]\rho'\,d\phi'\,d\rho', \tag{78}$$

$$=zT_sE_0T_1e^{ikn(t+\alpha a)}e^{-ik\epsilon}\int_0^a e^{ik(1-n)\rho'\alpha}\times\frac{e^{ikR}}{R^2}\left[\frac{1}{R}-ik\right]\rho'\,d\rho', \tag{79}$$

where $R=(\rho'^2+z^2)^{1/2}$.

The axial intensity $I(z)=|E_x(0,0,z)|^2$ is plotted in Fig. 9. It is seen that for increasing z, the intensity oscillates more strongly and then drops suddenly to zero. If we compare this with the scalar result [Eq. (21)], for the case of an incident plane wave, i.e., for a beam waist $w_0\gg a$, the two results are virtually indistinguishable. This should not come as a surprise: in the paraxial regime that we are dealing with, with a base angle $\alpha=1°$, we expect the scalar case to give results that are similar to those for a linearly polarized field.

This situation is quite different for incident beams with a nonuniform state of polarization. For an incident beam that is radially polarized, we find that applying the output field given by Eq. (68) to the diffraction integral of Eq. (53), yields that both E_x and E_y are zero. As before, we neglect the z component of the electric field. For an incident beam that is azimuthally polarized, substitution from Eq. (77) into Eq. (53) yields that all three components of the electric are zero for points along the central axis. Hence, we conclude that the axial intensity is nonzero when the incident beam is uniformly polarized, whereas it is zero for an incident beam with radial or azimuthal polarization.

B. Effective Wavelength on Axis

The rays that are refracted by the axicon all propagate under an angle $\beta-\alpha$ with the central axis (see Fig. 1). We therefore

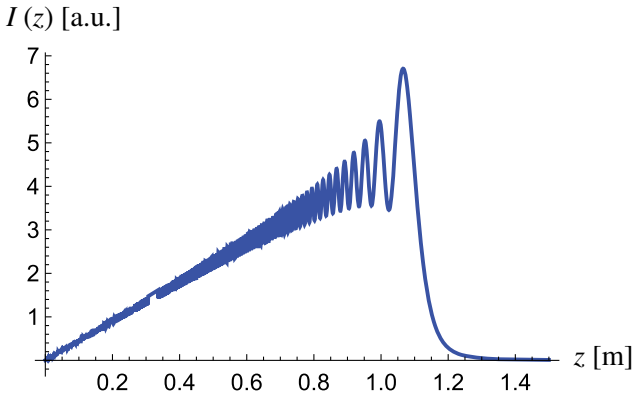

Fig. 9. Axial intensity distribution $I(z)=|E_x(0,0,z)|^2$ for an incident beam that x-polarized, as given by Eq. (79). In this example $n=1.5$, $a=1$ cm, $\alpha=1°$, and $\lambda=632.8$ nm.

Table 1. Effective Wavelength on Axis for an Incident Beam with $\lambda = 632.80$ nm

Base Angle α	Eq. (80) [nm]	Eq. (79) [nm]
1.0°	632.82	632.83
2.5°	632.95	632.95
5.0°	633.41	633.37

expect the effective axial wavelength λ_{eff} to be given by the expression

$$\lambda_{\text{eff}} = \frac{\lambda}{\cos(\beta - \alpha)}, \tag{80}$$

with λ the free-space wavelength of the incident field. We can verify this prediction by numerically determining the successive zeros of the argument (or phase) of $E_x(0, 0, z)$, using Eq. (79). This was done for three different values of the axicon base angle α, at a position halfway along the focal line, i.e., at $z = L/2$ [see Eq. (1)]. The results are shown in Table 1, and indicate an excellent agreement within the paraxial regime. This is in contrast with findings reported earlier for focusing systems with a much higher angular aperture [37,38].

C. Transverse Intensity

Scalar theory, using the method of stationary phase, predicts a normalized transverse intensity profile that is given by Eq. (26):

$$I(\rho) = \{J_0[(n-1)k\rho\alpha]\}^2, \qquad (z < L), \tag{81}$$

which is independent of z. If one does not make use of the stationary phase approximation, scalar theory predicts a more complex behavior, as illustrated by Figs. 5–8. On the other hand, the electromagnetic analysis for a linearly polarized beam leads to Eq. (55), from which we find for the only nonzero field component that

$$E_x(\mathbf{r}) = \frac{-1}{2\pi}\int_{z'=0} E_x^{(\text{out})}(\mathbf{r}')\partial_z \frac{e^{ikR}}{R}\mathrm{d}^2 r', \tag{82}$$

$$= -z\frac{T_s E_0 T_1}{2\pi} e^{ikn(t+\alpha a)} e^{-ik\epsilon} \times \int_0^a \int_0^{2\pi} e^{ik\rho'\alpha(1-n)} \frac{e^{ikR}}{R^2}[ik - 1/R]\rho' \mathrm{d}\phi' \mathrm{d}\rho', \tag{83}$$

with

$$R = \sqrt{(x - \rho'\cos\phi')^2 + (y - \rho'\sin\phi')^2 + z^2}. \tag{84}$$

The results of a numerical evaluation of Eq. (83) are, just as for the axial intensity, practically indistinguishable from the scalar results for a large beam waist that were presented in Section 3.

The transverse field for the radially polarized case is obtained by substituting Eq. (68) into Eq. (53). The resulting expressions are

$$E_x(\mathbf{r}) = \frac{-zT_s}{2\pi}\int_0^a \int_0^{2\pi} \Lambda(\rho')\cos\phi' e^{ik\rho'\alpha}(ik - 1/R) \times \frac{e^{ikR}}{R^2}\rho' \mathrm{d}\phi' \mathrm{d}\rho', \tag{85}$$

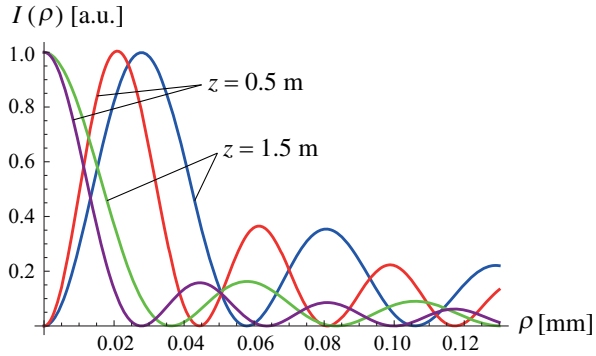

Fig. 10. Transverse intensity distribution for an incident beam that is x-polarized [Eq. (83)] (purple and green curves), and for a radially polarized [Eqs. (85) and (86)] or azimuthally polarized beam [Eqs. (87) and (88)] (red and blue curves), for $z = 0.5$ m and $z = 1.5$ m. The other parameters are $n = 1.5$, $a = 1$ cm, $\alpha = 1°$, and $\lambda = 632.8$ nm.

$$E_y(\mathbf{r}) = \frac{-zT_s}{2\pi}\int_0^a \int_0^{2\pi} \Lambda(\rho')\sin\phi' e^{ik\rho'\alpha}(ik - 1/R) \times \frac{e^{ikR}}{R^2}\rho' \mathrm{d}\phi' \mathrm{d}\rho'. \tag{86}$$

The transverse field for the azimuthally polarized case is obtained by substituting Eq. (77) into Eq. (53). One then finds that

$$E_x(\mathbf{r}) = \frac{zT_s}{2\pi}\int_0^a \int_0^{2\pi} \Lambda(\rho')\sin\phi' e^{ik\rho'\alpha}(ik - 1/R) \times \frac{e^{ikR}}{R^2}\rho' \mathrm{d}\phi' \mathrm{d}\rho', \tag{87}$$

$$E_y(\mathbf{r}) = \frac{-zT_s}{2\pi}\int_0^a \int_0^{2\pi} \Lambda(\rho')\cos\phi' e^{ik\rho'\alpha}(ik - 1/R) \times \frac{e^{ikR}}{R^2}\rho' \mathrm{d}\phi' \mathrm{d}\rho'. \tag{88}$$

On comparing Eqs. (87) and (88) with Eqs. (85) and (86), it is seen that an azimuthally polarized beam and a radially polarized beam produce exactly the same transverse intensity distribution. The transverse intensity distributions for a radially or azimuthally polarized beam and a linearly polarized beam are compared in Fig. 10. The radially and azimuthally polarized beams produce identical fields with a dark core that is surrounded by rings of decreasing intensity. When the plane of observation is changed from $z = 0.5$ m to $z = 1.5$ m, the central peak of the linearly polarized field broadens (purple and green curves), whereas the first peak of the radially or azimuthally polarized field is seen to move outward (red and blue curves).

D. Far-Zone Intensity

Far away from the output plane, Eq. (53) for the diffracted field takes the asymptotic form (Eq. 10.109, [35])

$$\mathbf{E}(r\hat{\mathbf{r}}) = ik\frac{e^{ikr}}{2\pi r}\hat{\mathbf{r}} \times \int_{z'=0} \hat{\mathbf{z}} \times \mathbf{E}^{(\text{out})}(\mathbf{r}')e^{-ik\hat{\mathbf{r}}\cdot\mathbf{r}'}\mathrm{d}^2 r'. \tag{89}$$

A derivation of Eq. (89) can be found in Appendix B. On defining the integrals

$$\mathcal{E}_i(r\hat{\mathbf{r}}) = \mathrm{i}k\frac{e^{\mathrm{i}kr}}{2\pi r}\int_{z'=0} E_i^{(\mathrm{out})}(\mathbf{r}')e^{-\mathrm{i}k\hat{\mathbf{r}}\cdot\mathbf{r}'}\mathrm{d}^2r'(i=x,y,z), \quad (90)$$

where the unit vector corresponding to the direction of observation is given by

$$\hat{\mathbf{r}} = (\sin\theta\cos\phi, \sin\theta\sin\phi, \cos\theta)^T, \quad (91)$$

we can derive, with $\mathbf{E}^{(\mathrm{out})}(\mathbf{r}')$ given by Eq. (52), that

$$\mathbf{E}(r\hat{\mathbf{r}}) = \begin{pmatrix} -\cos\theta\mathcal{E}_x(r\hat{\mathbf{r}}) \\ 0 \\ \sin\theta\cos\phi\mathcal{E}_x(r\hat{\mathbf{r}}) \end{pmatrix}. \quad (92)$$

Because of the assumption of paraxiality, we have that $\sin\theta \ll \cos\theta$, and the z component of the field may again be neglected. On substituting Eq. (52) into the definition of Eq. (90), we obtain the expression

$$\mathcal{E}_x(r\hat{\mathbf{r}}) = \mathrm{i}k\frac{e^{\mathrm{i}kr}}{2\pi r}T_s\int_0^a e^{\mathrm{i}k\rho'\alpha}\Lambda(\rho')\rho' \times\left\{\int_0^{2\pi} e^{-\mathrm{i}k\rho'\sin\theta\cos(\phi'-\phi)}\mathrm{d}\phi'\right\}\mathrm{d}\rho', \quad (93)$$

$$= \mathrm{i}k\frac{e^{\mathrm{i}kr}}{r}T_sT_1E_0e^{\mathrm{i}kn(t+\alpha a)}e^{-\mathrm{i}k\epsilon} \times\int_0^a e^{\mathrm{i}k\rho'\alpha(1-n)}\rho'J_0(k\rho'\sin\theta)\mathrm{d}\rho'. \quad (94)$$

The far-zone intensity

$$I(\theta) = |E_x(r\hat{\mathbf{r}})|^2 = \cos^2\theta|\mathcal{E}_x(r\hat{\mathbf{r}})|^2, \quad (95)$$

is plotted in Fig. 11 as a function of the angle θ. The intensity is seen to be sharply peaked, corresponding to a thin, ring-like distribution. In this case, the ring subtends an angle $\theta = 0.0087$ at the origin. We note that this is in exact agreement with the geometrical angle of refraction $\beta - \alpha$, as depicted in Fig. 1.

When the incident beam is radially polarized, substitution from Eq. (68) into Eq. (89) yields

$$\mathbf{E}(r\hat{\mathbf{r}}) = \begin{pmatrix} -\cos\theta\mathcal{E}_x(r\hat{\mathbf{r}}) \\ -\cos\theta\mathcal{E}_y(r\hat{\mathbf{r}}) \\ 0 \end{pmatrix}, \quad (96)$$

where

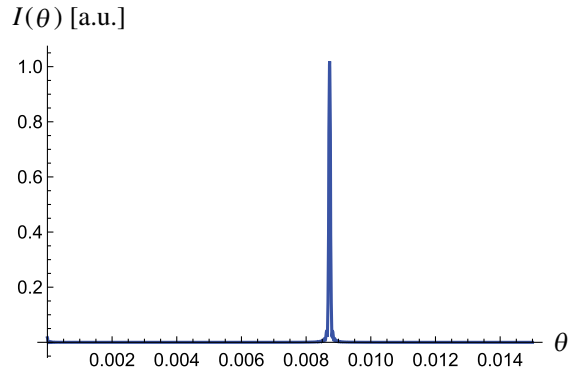

Fig. 11. Far-zone intensity distribution $I(\theta)$ as given by Eq. (95) for an incident beam that is x-polarized. In this example, $n = 1.5$, $a = 1$ cm, $\alpha = 1°$, and $\lambda = 632.8$ nm.

$$\mathcal{E}_x(r\hat{\mathbf{r}}) = k\frac{e^{\mathrm{i}kr}}{r}T_sT_1E_0e^{\mathrm{i}kn(t+\alpha a)}e^{-\mathrm{i}k\epsilon}\cos\phi \times\int_0^a e^{\mathrm{i}k\rho'\alpha(1-n)}\rho'J_1(k\rho'\sin\theta)\mathrm{d}\rho', \quad (97)$$

$$\mathcal{E}_y(r\hat{\mathbf{r}}) = k\frac{e^{\mathrm{i}kr}}{r}T_sT_1E_0e^{\mathrm{i}kn(t+\alpha a)}e^{-\mathrm{i}k\epsilon}\sin\phi \times\int_0^a e^{\mathrm{i}k\rho'\alpha(1-n)}\rho'J_1(k\rho'\sin\theta)\mathrm{d}\rho'. \quad (98)$$

It is clear from the ϕ dependence in Eqs. (97) and (98) that the far-zone field is radially polarized, as is to be expected.

In a similar fashion, we find on substituting from Eq. (77) into Eq. (89) that for an azimuthally polarized beam

$$\mathbf{E}(r\hat{\mathbf{r}}) = \begin{pmatrix} \cos\theta\mathcal{E}_x(r\hat{\mathbf{r}}) \\ \cos\theta\mathcal{E}_y(r\hat{\mathbf{r}}) \\ 0 \end{pmatrix}, \quad (99)$$

with

$$\mathcal{E}_x(r\hat{\mathbf{r}}) = -k\frac{e^{\mathrm{i}kr}}{r}T_sT_1E_0e^{\mathrm{i}kn(t+\alpha a)}e^{-\mathrm{i}k\epsilon}\sin\phi \times\int_0^a e^{\mathrm{i}k\rho'\alpha(1-n)}\rho'J_1(k\rho'\sin\theta)\mathrm{d}\rho', \quad (100)$$

$$\mathcal{E}_y(r\hat{\mathbf{r}}) = k\frac{e^{\mathrm{i}kr}}{r}T_sT_1E_0e^{\mathrm{i}kn(t+\alpha a)}e^{-\mathrm{i}k\epsilon}\cos\phi \times\int_0^a e^{\mathrm{i}k\rho'\alpha(1-n)}\rho'J_1(k\rho'\sin\theta)\mathrm{d}\rho'. \quad (101)$$

It is seen from Eqs. (100) and (101) that this field is indeed azimuthally polarized. A comparison of Eqs. (96) and (99) shows that the far-zone intensity produced by radially polarized and azimuthally polarized beams are identical. Moreover, a numerical evaluation shows that the far-zone intensity distribution for these two types of polarization is the same as that for a linearly polarized beam shown in Fig. 11. This may seem somewhat counterintuitive, because Eq. (94) involves a J_0 function, whereas the corresponding expressions for the radial and azimuthal cases contain a J_1 function. However, the respective integrands are all products of two rapidly oscillating functions, namely an exponent and a J_0 or a J_1 Bessel function. Loosely speaking, these oscillations will tend to cancel each other, except when they occur in unison. This happens when the functional arguments are equal, i.e., when $-k\rho'\alpha(1-n) = k\rho'\sin\theta$, which implies that these integrals will all be approximately zero except when $\sin\theta = \beta - \alpha$. This is precisely the geometrical angle of refraction that was mentioned above in connection with Fig. 11.

6. CONCLUSION

We have analyzed the field of a paraxial refractive axicon within the frameworks of geometrical optics, scalar optics, and electromagnetic optics. The field along the central axis and the transition to a ring-like distribution were examined. It was shown that the scalar theory and the electromagnetic theory are in very good agreement for the case of an incident beam that is linearly polarized. However, scalar theory cannot describe the field that is produced when the incident beam is radially polarized or azimuthally polarized. In those two latter cases, the axial intensity

is zero, and the transverse intensity is a field with a dark core surrounded by rings of decreasing intensity. In the far zone, the axicon produces a ring-like field whose intensity distribution is independent of the state of polarization of the incident field.

APPENDIX A:DERIVATION OF EQ. (23)

In this appendix, the stationary-phase calculation of the axicon field is outlined (cf. [39]). We note that this method applies to systems for which the Fresnel number $N = a^2/(\lambda L) \gg 1$; see [24]. To this end, let us assume that $f(\rho')$ and $g(\rho')$ are two well-behaved functions in an integral in the form of

$$F(k) = \int_0^a f(\rho') \exp[\mathrm{i}kg(\rho')]\mathrm{d}\rho'. \tag{A1}$$

If k tends to infinity, the general solution of this integral is ([28], Section 3.3)

$$F(k) \sim \left(\frac{2\pi}{k}\right)^{1/2} \frac{\exp(\pm \mathrm{i}\pi/4)}{|g''(\rho_c')|^{1/2}} f(\rho_c') \exp[\mathrm{i}kg(\rho_c')], (k \to \infty), \tag{A2}$$

where ρ_c' is known as the critical point, which is obtained when the derivative of $g(\rho')$ is zero, i.e., $g'(\rho') = 0$. From comparing Eqs. (21) and (A1), it is clear that

$$f(\rho') = \exp(-\rho'^2/w_0^2) J_0\left(\frac{k\rho\rho'}{z}\right)\rho', \tag{A3}$$

$$g(\rho') = (1-n)\rho'\alpha + \frac{\rho'^2}{2z}. \tag{A4}$$

Thus, the derivatives of $g(\rho')$ are

$$g'(\rho') = (1-n)\alpha + \frac{\rho'}{z}, \tag{A5}$$

$$g''(\rho') = \frac{1}{z}. \tag{A6}$$

The fact that $g''(\rho') > 0$ implies that the plus sign must be chosen in Eq. (A2). It follows immediately from Eq. (A5) that the critical point

$$\rho_c' = z(n-1)\alpha. \tag{A7}$$

Substitution from Eqs. (A3), (A4), and (A6) into Eq. (A2) yields Eq. (23). Notice that the interior critical point is confined to the range of integration, i.e.,

$$0 \le \rho_c' \le a. \tag{A8}$$

This means, according to Eq. (A7), that the method of stationary phase predicts a field that is identically zero when

$$z > \frac{a}{\alpha(n-1)}. \tag{A9}$$

As is well known, geometrical optics may be regarded as the asymptotic limit of physical optics as the wavenumber k tends to infinity ([27], Section 3.1). Therefore, Eq. (A2) reproduces the geometrical optics result that the field is zero when z exceeds the focal line length L. It is easily verified numerically that L, as given by Eq. (1), is indeed very well approximated by the right-hand side of the inequality (A9).

APPENDIX B:DERIVATION OF EQ. (89)

We begin by applying a product rule to Eq. (53), namely,

$$\nabla \times (\mathbf{A} \times \mathbf{B}) = \mathbf{A}(\nabla \cdot \mathbf{B}) - (\mathbf{A} \cdot \nabla)\mathbf{B} + (\mathbf{B} \cdot \nabla)\mathbf{A} - \mathbf{B}(\nabla \cdot \mathbf{A}). \tag{A10}$$

Since $\mathbf{A} = \hat{\mathbf{z}}$ is a constant vector, the third and fourth terms are both zero. Furthermore,

$$\nabla \cdot \mathbf{B} = \nabla \cdot \left(\mathbf{E}^{(\mathrm{out})}(\mathbf{r}')\frac{e^{\mathrm{i}kR}}{R}\right), \tag{A11}$$

$$= E_x^{(\mathrm{out})}(\mathbf{r}')\partial_x \frac{e^{\mathrm{i}kR}}{R} + E_y^{(\mathrm{out})}(\mathbf{r}')\partial_y \frac{e^{\mathrm{i}kR}}{R} + E_z^{(\mathrm{out})}(\mathbf{r}')\partial_z \frac{e^{\mathrm{i}kR}}{R}, \tag{A12}$$

$$= \frac{E_x^{(\mathrm{out})}(\mathbf{r}')e^{\mathrm{i}kR}[\mathrm{i}k(x-x') - (x-x')/R]}{R^2} + \frac{E_y^{(\mathrm{out})}(\mathbf{r}')e^{\mathrm{i}kR}[\mathrm{i}k(y-y') - (y-y')/R]}{R^2} + \frac{E_z^{(\mathrm{out})}(\mathbf{r}')e^{\mathrm{i}kR}[\mathrm{i}kz - z/R]}{R^2}. \tag{A13}$$

Because in the far zone $R \gg \lambda$, we may write

$$\nabla \cdot \mathbf{B} = \frac{E_x^{(\mathrm{out})}(\mathbf{r}')\mathrm{i}k(x-x')e^{\mathrm{i}kR}}{R^2} + \frac{E_y^{(\mathrm{out})}(\mathbf{r}')\mathrm{i}k(y-y')e^{\mathrm{i}kR}}{R^2} + \frac{E_z^{(\mathrm{out})}(\mathbf{r}')\mathrm{i}kze^{\mathrm{i}kR}}{R^2}. \tag{A14}$$

Thus, the first term on the right-hand side of Eq. (A10) becomes

$$\mathbf{A}(\nabla \cdot \mathbf{B}) = \hat{\mathbf{z}}\left[\frac{E_x^{(\mathrm{out})}(\mathbf{r}')\mathrm{i}k(x-x')e^{\mathrm{i}kR}}{R^2} + \frac{E_y^{(\mathrm{out})}(\mathbf{r}')\mathrm{i}k(y-y')e^{\mathrm{i}kR}}{R^2} + \frac{E_z^{(\mathrm{out})}(\mathbf{r}')\mathrm{i}kze^{\mathrm{i}kR}}{R^2}\right]. \tag{A15}$$

For the second term of Eq. (A10) we have that

$$-(\mathbf{A} \cdot \nabla)\mathbf{B} = -\mathbf{E}^{(\mathrm{out})}(\mathbf{r}')\partial_z \frac{e^{\mathrm{i}kR}}{R}. \tag{A16}$$

Making again use of the fact that $R \gg \lambda$, we obtain the result

$$-(\mathbf{A} \cdot \nabla)\mathbf{B} = -\mathbf{E}^{(\mathrm{out})}(\mathbf{r}')\mathrm{i}kz\frac{e^{\mathrm{i}kR}}{R^2}. \tag{A17}$$

Thus, we can rewrite Eq. (53) as

$$\mathbf{E}(r\hat{\mathbf{r}}) = \frac{\mathrm{i}k}{2\pi}\int_{z'=0} \{\hat{\mathbf{z}}[E_x^{(\mathrm{out})}(\mathbf{r}')(x-x') + E_y^{(\mathrm{out})}(\mathbf{r}')(y-y') + E_z^{(\mathrm{out})}(\mathbf{r}')z] - \mathbf{E}^{(\mathrm{out})}(\mathbf{r}')(\hat{\mathbf{z}} \cdot \mathbf{r})\}\frac{e^{\mathrm{i}kR}}{R^2}\mathrm{d}^2r'. \tag{A18}$$

Because x' and y' are bounded by the size of the axicon radius a, we may neglect the terms in x' and y' as $R \to \infty$. Also,

we use that in that limit $kR \approx kr - k\hat{\mathbf{r}}\cdot\mathbf{r}'$, and that $1/R^2 \approx 1/r^2$. This yields

$$\mathbf{E}(r\hat{\mathbf{r}}) = \frac{\mathrm{i}ke^{\mathrm{i}kr}}{2\pi r^2}\int_{z'=0}\{\hat{\mathbf{z}}[E_x^{(\mathrm{out})}(\mathbf{r}')x + E_y^{(\mathrm{out})}(\mathbf{r}')y + E_z^{(\mathrm{out})}(\mathbf{r}')z] - \mathbf{E}^{(\mathrm{out})}(\mathbf{r}')(\hat{\mathbf{z}}\cdot\mathbf{r})\}e^{-\mathrm{i}k\hat{\mathbf{r}}\cdot\mathbf{r}'}\mathrm{d}^2r', \quad \textbf{(A19)}$$

$$= \frac{\mathrm{i}ke^{\mathrm{i}kr}}{2\pi r}\int_{z'=0}[\hat{\mathbf{z}}(\mathbf{E}^{(\mathrm{out})}(\mathbf{r}')\cdot\hat{\mathbf{r}}) - \mathbf{E}^{(\mathrm{out})}(\mathbf{r}')(\hat{\mathbf{z}}\cdot\hat{\mathbf{r}})]e^{-\mathrm{i}k\hat{\mathbf{r}}\cdot\mathbf{r}'}\mathrm{d}^2r'. \quad \textbf{(A20)}$$

Using the "BAC-CAB" rule

$$\mathbf{A}\times(\mathbf{B}\times\mathbf{C}) = \mathbf{B}(\mathbf{A}\cdot\mathbf{C}) - \mathbf{C}(\mathbf{A}\cdot\mathbf{B}), \quad \textbf{(A21)}$$

we finally obtain the formula

$$\mathbf{E}(r\hat{\mathbf{r}}) = \frac{\mathrm{i}ke^{\mathrm{i}kr}}{2\pi r}\hat{\mathbf{r}}\times\int_{z'=0}\hat{\mathbf{z}}\times\mathbf{E}^{(\mathrm{out})}(\mathbf{r}')e^{-\mathrm{i}k\hat{\mathbf{r}}\cdot\mathbf{r}'}\mathrm{d}^2r', \quad \textbf{(A22)}$$

which is Eq. (89).

Funding. Air Force Office of Scientific Research (AFOSR) (FA9550-16-1-0119).

Acknowledgment. T. D. V. also acknowledges support from the Joensuu University Foundation. Y. W. is supported by the Excellent Doctorate Foundation of Northwestern Polytechnical University.

REFERENCES

1. J. H. McLeod, "The axicon: a new type of optical element," J. Opt. Soc. Am. **44**, 592–597 (1954).
2. J. Sochacki, A. Kolodziejczyk, Z. Jaroszewicz, and S. Bara, "Nonparaxial design of generalized axicons," Appl. Opt. **31**, 5326–5330 (1992).
3. S. Brinkmann, T. Dresel, R. Schreiner, and J. Schwider, "Axicon-type test interferometer for cylindrical surfaces," in *Simulation and Experiment in Laser Metrology*, Z. Füzessy, W. Jüptner, and W. Osten, eds. (Akademie Verlag, 1996), pp. 82–87.
4. I. Velchev and W. Ubachs, "Higher-order stimulated Brillouin scattering with nondiffracting beams," Opt. Lett. **26**, 530–532 (2001).
5. F. P. Schafer, "On some properties of axicons," Appl. Phys. B **39**, 1–8 (1986).
6. M. Rioux, R. Tremblay, and P. A. Bélanger, "Linear, annular, and radial focusing with axicons and applications to laser machining," Appl. Opt. **17**, 1532–1536 (1978).
7. B. Shao, S. C. Esener, J. M. Nascimento, E. L. Botvinick, and M. W. Berns, "Dynamically adjustable annular laser trapping based on axicons," Appl. Opt. **45**, 6421–6428 (2006).
8. T. Wulle and S. Herminghaus, "Nonlinear optics of Bessel beams," Phys. Rev. Lett. **70**, 1401–1404 (1993).
9. G. Bickel, G. Hausler, and M. Haul, "Triangulation with expanded range of depth," Opt. Eng. **24**, 975–977 (1985).
10. Z. Ding, H. Ren, Y. Zhao, J. S. Nelson, and Z. Chen, "High-resolution optical coherence tomography over a large depth range with an axicon lens," Opt. Lett. **27**, 243–245 (2002).
11. Q. Ren and R. Birngruber, "Axicon: a new laser beam delivery system for corneal surgery," IEEE J. Quantum Electron. **26**, 2305–2308 (1990).
12. H. E. Hernandez-Figueroa, E. Recami, and M. Zamboni-Rached, eds., *Non-Diffracting Waves* (Wiley, 2014).
13. L. M. Soroko, "Axicons and meso-optical imaging devices," Vol. **27** of *Progress in Optics*, E. Wolf, ed. (Elsevier, 1989), pp. 109–160.
14. Z. Jaroszewicz, *Axicons-Design and Propagation Properties* (SPIE, 1997).
15. Z. Jaroszewicz, A. Burvall, and A. T. Friberg, "Axicon-the most important optical element," Opt. Photon. News **16**(4), 34–39 (2005).
16. W. R. Edmonds, "Imaging properties of a conic axicon," Appl. Opt. **13**, 1762–1764 (1974).
17. J. Durnin, J. J. Miceli, Jr., and J. H. Eberly, "Diffraction-free beams," Phys. Rev. Lett. **58**, 1499–1501 (1987).
18. J. Tervo and J. Turunen, "Generation of vectorial propagation-invariant fields by polarization-grating axicons," Opt. Commun. **192**, 13–18 (2001).
19. S. Fujiwara, "Optical properties of conic surfaces. I. Reflecting cone," J. Opt. Soc. Am. **52**, 287–292 (1962).
20. J. Turunen and A. T. Friberg, "Electromagnetic theory of reflaxicon fields," Pure Appl. Opt. **2**, 539–547 (1993).
21. R. Dutta, K. Saastamoinen, J. Turunen, and A. T. Friberg, "Broadband spatiotemporal axicon fields," Opt. Express **22**, 25015–25026 (2014).
22. N. Radwell, R. D. Hawley, J. B. Gotte, and S. Franke-Arnold, "Achromatic vector vortex beams from a glass cone," Nat. Commun. **7**, 10564 (2016).
23. J. H. McLeod, "Axicons and their uses," J. Opt. Soc. Am. **50**, 166–169 (1960).
24. C. J. Zapata-Rodriguez and A. Sanchez-Losa, "Three-dimensional field distribution in the focal region of low-Fresnel-number axicons," J. Opt. Soc. Am. A **23**, 3016–3026 (2005).
25. B. Richards and E. Wolf, "Electromagnetic diffraction in optical systems. II. Structure of the image field in an aplanatic system," Proc. R. Soc. London A **253**, 358–379 (1959).
26. T. G. Brown, "Unconventional polarization states: beam propagation, focusing, and imaging," Vol. **56** of *Progress in Optics*, E. Wolf, ed. (Elsevier, 2011), pp. 81–129.
27. M. Born and E. Wolf, *Principles of Optics*, 7th ed. (Cambridge University, 1995).
28. L. Mandel and E. Wolf, *Optical Coherence and Quantum Optics* (Cambridge University, 1995).
29. Z. L. Horvath and Z. Bor, "Diffraction of short pulses with boundary diffraction wave theory," Phys. Rev. E **63**, 026601 (2001).
30. J. Turunen, A. Vasara, and A. T. Friberg, "Holographic generation of diffraction-free beams," Appl. Opt. **27**, 3959–3962 (1988).
31. A. Vasara, J. Turunen, and A. T. Friberg, "Realization of general nondiffracting beams with computer-generated holograms," J. Opt. Soc. Am. A **6**, 1748–1754 (1989).
32. J. Turunen and A. T. Friberg, "Self-imaging and propagation-invariance in electromagnetic fields," Pure Appl. Opt. **2**, 51–60 (1993).
33. J. Turunen and A. T. Friberg, "Propagation-invariant optical fields," Vol. **54** of *Progress in Optics*, E. Wolf, ed. (Elsevier, 2009), pp. 1–88.
34. U. Levy, S. Derevyanko, and Y. Silberberg, "Light modes of free space," Vol. **61** of *Progress in Optics*, T. D. Visser, ed. (Elsevier, 2016), pp. 237–281.
35. J. D. Jackson, *Classical Electrodynamics*, 3rd ed. (Wiley, 1998).
36. G. Toraldo di Francia, *Electromagnetic Waves* (Interscience, 1955).
37. J. T. Foley and E. Wolf, "Wave-front spacing in the focal region of high-numerical-aperture systems," Opt. Lett. **30**, 1312–1314 (2005).
38. T. D. Visser and J. T. Foley, "On the wavefront spacing of focused, radially polarized beams," J. Opt. Soc. Am. A **22**, 2527–2531 (2005).
39. A. T. Friberg, "Stationary phase analysis of generalized axicons," J. Opt. Soc. Am. A **13**, 743–750 (1996).